Electronic structure, magnetism, and high-temperature superconductivity in multilayer octagraphene and octagraphite

Jun Li (李军) [1], Shangjian Jin (金尚健) [1], Fan Yang (杨帆),[2] and Dao-Xin Yao (姚道新) [1,*]

[1]*State Key Laboratory of Optoelectronic Materials and Technologies,*
School of Physics, Sun Yat-Sen University, Guangzhou 510275, Peoples Republic of China
[2]*School of Physics, Beijing Institute of Technology, Beijing 100081, China*

We systematically investigate the electronic structure, magnetism, and high-temperature superconductivity (SC) in multilayer octagraphene and octagraphite (bulk octagraphene). A tight-binding model is used to fit the electronic structures of single-layer and multilayer octagraphenes and octagraphite. We find that multilayer octagraphene and octagraphite follow a simple A-A stacking structure from the energy analysis. The van der Waals interaction induces $t_\perp \approx 0.25$ eV and the hopping integral within each layer changes little when the layer number n increases. There is a well Fermi-surface nesting with nesting vector $\mathbf{Q} = (\pi, \pi)$ for single-layer octagraphene at half-filling, which can induce a two-dimensional Néel antiferromagnetic order. With increasing layer number $n \to \infty$, the Fermi-surface nesting transforms to three-dimensional (3D) with nesting vector $\mathbf{Q} = (\pi, \pi, \pi)$ and shows that the system has a 3D Néel antiferromagnetic order. Upon doping, multilayer octagraphene and octagraphite can enter a high-temperature $s^\pm$ SC driven by spin fluctuation. We evaluate the superconducting transition temperature T_c by using the random-phase approximation, which yields a high T_c even if the layer number $n \geqslant 3$. Our study shows that multilayer octagraphene and octagraphite are promising candidates for realizing high-temperature SC.

I. INTRODUCTION

Two-dimensional (2D) superconductors (SCs) have drawn tremendous interest for their rich physical properties and potential applications. So far, SCs have been reported in many 2D materials, such as FeSe-SrTiO$_3$ [1], monolayer NbSe$_2$ [2], MoS$_2$ [3], CuO$_2$ [4], and Bi$_2$Sr$_2$CaCu$_2$O$_{8+\delta}$ [5]. As the first single-layer 2D material, graphene [6] shows an interesting proximity-induced superconductivity when it contacts SC materials [7]. Besides, few-layer graphene with doping may exhibit a considerable superconducting transition temperature T_c [8–12], which is higher than the reported T_c in bulk compounds of the same composition [13]. Recently, "high-temperature SC" with a $T_c \sim 1.7$ K has been revealed in magic-angle twisted bilayer graphene [14]. This progress informs us that combinations and interactions between layers may have important influences on the properties of 2D materials.

Theoretically, the SC of graphene-based 2D materials has been widely studied via the Eliashberg theory under the framework of the electron-phonon coupling mechanism (BCS) [15–20]. By doping and applying a biaxial stress, the highest T_c of graphene-based materials has been proposed to reach 30 K [19]. In addition to graphene, variable forms of graphyne have been predicted and some synthesized [21]. It is only predicted that α-graphyne would exhibit a SC with $T_c \sim 12$ K by hole-doping and biaxial tensile strain [22].

The hexagonal symmetry of graphene or graphyne is unfavorable to form Fermi surface nesting with a high density of states, which is important to form high-temperature superconductivity.

Another 2D carbon-based material is octagraphene [23–25]. Astonishingly, the 2D square-octagon lattice structure of single-layer octagraphene leads to a high density of states near the well-nested Fermi surface (FS), which may induce an antiferromagnetic spin-density-wave order. The BCS mechanism based on electron-phonon interaction is not enough to describe the pairing and the SC mainly originates from spin fluctuation. Our recent research on a repulsive Hubbard model on a square-octagon lattice with nearest-neighbor and next-nearest-neighbor hopping terms, which can serve as a rough representation of single-layer octagraphene, shows that the system can host a high-temperature SC with $s^\pm$-wave pairing symmetry [26]. Unlike the complex forms of other 2D superconductors, the simple structure of octagraphene may be an ideal platform for studying the origin of high-temperature SCs. In real materials, multilayer octagraphene and octagraphite may be more common. We here study the electronic structures, magnetism, and high-temperature superconductivity in multilayer octagraphene and octagraphite.

Meanwhile, the dynamical stability of octagraphene (in some papers, it is called T-graphene) is confirmed by DFT calculation [23–25,27]. The synthesizations of octagraphene, multi-layer octagraphene and octagraphite are in progress. While a novel synthesization route of single-layer octagraphene has been proposed theoretically [27],
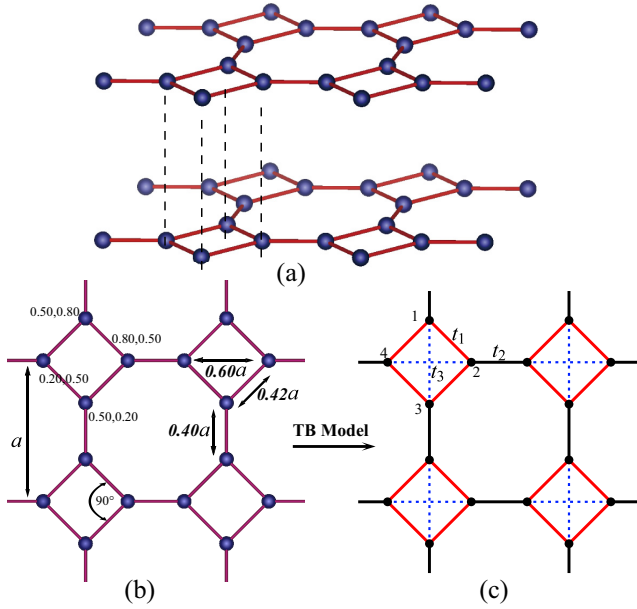
*yaodaox@mail.sysu.edu.cn

FIG. 1. (a) Predicted structure of octagraphene from DFT calculation. The relative positions between the layers form an A-A stacking. (b) Structure of single-layer octagraphene. The relative positions of four carbon atoms in a unit cell are independent of the deformation. (c) Two-dimensional single-orbital TB model. t_1, t_2, and t_3 correspond to the intrasquare, intersquare, and diagonal hopping energies, respectively.

an one-dimensional carbon nanoribbons with partial four and eight-membered rings has been realized experimentally [28]. As octagraphene shows a low cohesive energy [24], it has an opportunity to build the strongest carbon atomic sheet after graphene.

In this paper, we get a better tight-binding (TB) model to study the band structure of single-layer octagraphene. In comparison with our previous work [26], the present Hamiltonian adopts hopping integrals fitted from the density-functional theory (DFT) calculations and are thus more realistic. Unlike the complex stacking of the graphene, our DFT calculation suggests that multilayer octagraphenes more likely build an A-A stacking [see Fig. 1(a)]. There is a well FS nesting with nesting vector $\mathbf{Q} = (\pi, \pi)$ for single-layer octagraphene at half-filling, which can induce 2D Néel antiferromagnetic order. With increasing layer number $n \to \infty$, the FS nesting transforms to 3D with nesting vector $\mathbf{Q} = (\pi, \pi, \pi)$ and shows that the system has 3D Néel antiferromagnetic order. Upon doping, multilayer octagraphene and octagraphite can enter a high-temperature $s^{\pm}$ SC driven by spin fluctuation. We calculate the T_c of single-layer octagraphene, multilayer octagraphene, and octagraphite and find that the interlayer interaction does not affect the superconducting state much. With increasing n, T_c converges to ~170 K, which is still high.

The rest of the paper is organized as follows. In Sec. II we provide our model and the details of our methods. In Sec. III, we introduce the calculations for single-layer octagraphene and compare them with our previous work. In Sec. IV, we study the properties of multilayer octagraphenes. Section V provides the results for octagraphite, which is different from

multilayer octagraphenes. The T_c obtained with increasing layer number n is given in our estimation. Finally, in Sec. VI we provide the conclusions.

II. MODEL AND APPROACH

A. The model

We use the projector-augmented wave method implemented in the Vienna Ab initio Simulation Package (VASP) to perform density-functional theory (DFT) calculations [29–32]. The generalized gradient approximation and the Perdew Burke-Ernzerhof (PBE) function are used to treat the electron exchange correlation potential [33]. The vacuum is set at 15 Å to avoid external interaction. Grimme's DFT-D3 is chosen to correct the van der Waals (vdW) interaction [34]. In some other systems, Grimme's DFT-D3 may be less accurate than other vdW functionals, such as optB88-vdW [35], vdWDF [36], vdWDF2 [37], and vdW-DF-cx [38,39]. However, in carbon systems, Grimme's DFT-D3 gives rather precise results. For example, the calculated relative error is only $\delta c \approx 0.4\%$ from the experimental lattice constants for graphite [27]. An extremely high cutoff energy (1500 eV) and $16 \times 16 \times 1$ k-point mesh with the Monkhorst-Pack scheme are used in the self-consistent calculation.

To quantitatively analyze the band structures from DFT calculations, we build a TB model to describe single-layer octagraphene, multilayer octagraphene, and octagraphite. The Hamiltonian can be expressed as

$$H_{\mathrm{TB}} = -\sum_{i,j,\sigma} t_{ij} c_{i\sigma}^{\dagger} c_{j\sigma} - \sum_{<i,j>} t_{\perp} c_i^{\dagger} c_j + \mathrm{H.c.}, \quad (1)$$

where $c_{i\sigma}^{\dagger}$ ($c_{i\sigma}$) is the electron creation (annihilation) operator for a given site i with spin σ, t_{ij} are the hopping energies defined in Fig. 1(c) and $t_{\perp}$ represents the van der Waals interlayer interaction between neighbor layers. Note that the matrix form of Eq. (1) is different for single-layer octagraphene, multilayer octagraphene, and octagraphite.

Similarly to graphene, there are strong Coulomb repulsions between the $2p_z$ electrons in octagraphene materials. Here we use an effective Hubbard model to describe the effects

$$H_{\mathrm{Hubbard}} = H_{\mathrm{TB}} + U \sum_i \hat{n}_{i\uparrow} \hat{n}_{i\downarrow}. \quad (2)$$

Here the U term represents the on-site repulsive Hubbard interaction between the $2p_z$ electrons within the same site.

B. The random-phase approximation (RPA) approach

We use the RPA procedure outlined in our prior work [26,40] to solve Eq. (2). Generally neglecting the frequency dependence, we define free susceptibility for $U = 0$,

$$\chi_{s,t}^{(0)p,q}(\mathbf{q})$$

$$= \frac{1}{N} \sum_{\mathbf{k},\alpha,\beta} \xi_t^{\alpha}(\mathbf{k}) \xi_s^{\alpha,*}(\mathbf{k}) \xi_q^{\beta}(\mathbf{k}') \xi_p^{\beta,*}(\mathbf{k}') \frac{n_F(\varepsilon_{\mathbf{k}'}^{\beta}) - n_F(\varepsilon_{\mathbf{k}}^{\alpha})}{\varepsilon_{\mathbf{k}}^{\alpha} - \varepsilon_{\mathbf{k}'}^{\beta}}, \quad (3)$$

where $\alpha, \beta = 1, 2, 3, 4$ are band indices, $\mathbf{q} = \mathbf{k}' - \mathbf{k}$ is the nesting vector between $\mathbf{k}'$ and $\mathbf{k}$, $\varepsilon_{\mathbf{k}}^{\alpha}$ and $\xi_{\xi}^{\alpha}(\mathbf{k})$ are the αth

eigenvalue and eigenvector of matrix form of Eq. (1), respectively, and n_F is the Fermi-Dirac distribution function.

At the RPA level, the spin (charge) susceptibility for the Hubbard model is

$$\chi^{(c(s))}(\mathbf{q}) = [I + (-)\chi^{(0)}(\mathbf{q})\widetilde{U}]^{-1}\chi^{(0)}(\mathbf{q}), \qquad (4)$$

where $\chi^{(c(s))}(\mathbf{q})$, $\chi^{(0)}(\mathbf{q})$, and $\widetilde{U}$ are 16×16 matrices with $\widetilde{U}_{st}^{pq} = U\delta_{s=t=p=q}$.

A Cooper pair with momentum $\mathbf{k}'$ and orbital (t, s) could be scattered to $\mathbf{k}$, (p, q) by charge or spin fluctuations. At the RPA level, to project the effective interaction into the two bands which cross the Fermi surface, we obtain the low-energy effective Hamiltonian for Cooper pairs near the Fermi surface

$$V_{\text{eff}} = \frac{1}{N} \sum_{\alpha\beta,\mathbf{kk}'} V^{\alpha\beta}(\mathbf{k}, \mathbf{k}')c_\alpha^\dagger(\mathbf{k})c_\alpha^\dagger(-\mathbf{k})c_\beta(-\mathbf{k}')c_\beta(\mathbf{k}'), \quad (5)$$

where $\alpha, \beta = 1, 2$ and $V^{\alpha\beta}$ is

$$V^{\alpha\beta}(\mathbf{k}, \mathbf{k}')$$
$$= \text{Re} \sum_{pqst,\mathbf{kk}'} \Gamma_{st}^{pq}(\mathbf{k}, \mathbf{k}', 0)\xi_p^{\alpha,*}(\mathbf{k})\xi_q^{\alpha,*}(-\mathbf{k})\xi_s^{\beta}(-\mathbf{k}')\xi_t^{\beta}(\mathbf{k}').$$
$$(6)$$

In the singlet channel, the effective vertex $\Gamma_{st}^{pq}(k, k')$ is given as

$$\Gamma_{st}^{pq}(k, k') = \widetilde{U}_{qs}^{pt} + \frac{1}{4}\{\widetilde{U}[3\chi^{(s)}(k - k') - \chi^{(c)}(k - k')]\widetilde{U}\}_{qs}^{pt}$$
$$+ \frac{1}{4}\{\widetilde{U}[3\chi^{(s)}(k + k') - \chi^{(c)}(k + k')]\widetilde{U}\}_{qt}^{ps},$$
$$(7)$$

while in the triplet channel, it is

$$\Gamma_{st}^{pq}(k, k') = -\frac{1}{4}\{\widetilde{U}[\chi^{(s)}(k - k') + \chi^{(c)}(k - k')]\widetilde{U}\}_{qs}^{pt}$$
$$+ \frac{1}{4}\{\widetilde{U}[\chi^{(s)}(k + k') + \chi^{(c)}(k + k')]\widetilde{U}\}_{qt}^{ps}. \quad (8)$$

We can construct the following linear integral gap equation to determine the T_c and the leading pairing symmetry of the system from the low-energy effective Hamiltonian, Eq. (5):

$$-\frac{1}{(2\pi)^2} \sum_\beta \oint_{FS} dk_\parallel' \frac{V^{\alpha\beta}(\mathbf{k}, \mathbf{k}')}{v_F^\beta(\mathbf{k}')}\Delta_\beta(\mathbf{k}') = \lambda\Delta_\alpha(\mathbf{k}). \quad (9)$$

Here, the integration and summation are along variable FS patches labeled α or β. v_F^β is the Fermi velocity at k' on the βth Fermi surface patch, and $\mathbf{k}'$, $\mathbf{k}$ represent the component along that patch. In the eigenvalue problem, the normalized eigenvector $\Delta_\alpha(\mathbf{k})$ represents the relative value of the gap function on the αth FS patch. The largest pairing eigenvalue λ is used to estimate T_c by the equation

$$\lambda^{-1} = \ln\left(1.13\frac{\hbar\omega_D}{k_B T_c}\right), \quad (10)$$

where we choose the typical energy scale of the spin fluctuation $\hbar\omega_D = 0.3$ eV in our calculation (see Ref. [40]). Although the RPA usually overestimates T_c because of its weak-coupling perturbation, we here use a smaller U than the actual situation to get the relatively credible T_c. In the previous calculation for single-layer octagraphene by using the variational Monte Carlo method [26], we get a similar
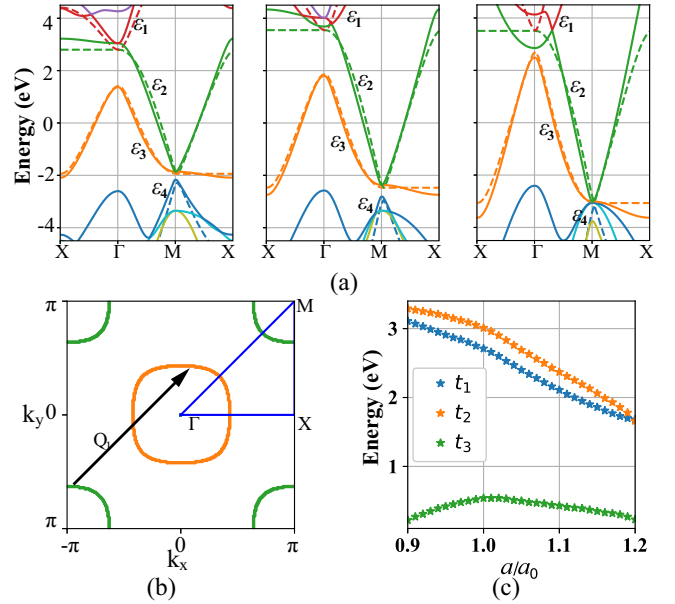

FIG. 2. Single-layer octagraphene. (a) Band structures of different lattice constants a: $a/a_0 = 1.1$, 1.0, and 0.9 ($a_0 = 3.44$ Å). DFT-calculated results, solid lines; fitting results obtained with the TB model, dashed lines. For $a/a_0 = 0.9$, the bands show a quadruple degeneracy at point M, with $E = -3.01$ eV. (b) Fermi surface from the TB model, independent of the relative lattice constant a/a_0. The Fermi surface is well nested by the vector $\mathbf{Q}_1 = (\pi, \pi)$. (c) Variable fitting parameters t_1, t_2, and t_3 of the TB model with lattice constant a. $t_2/t_1 = 1.1$ is almost constantly independent of a.

result with an optimized gap $\Delta \approx 50$ meV for $U = 10$ eV, which implies a similar T_c here.

III. SINGLE-LAYER OCTAGRAPHENE

In our DFT calculation of single-layer octagraphene, the fit of the Birch-Murnaghan equation of state gives the more accurate lattice constant $a_0 = 3.44$ Å. We note that the relative positions of carbon atoms are almost independent of the lattice constant a. The calculated square-octagon lattice is shown in Fig. 1(b). The positions of four carbon atoms in the unit cell are at $(0.50a, 0.20a)$, $(0.20a, 0.50a)$, $(0.50a, 0.80a)$, and $(0.80a, 0.50a)$, respectively, consistent with C_{4v} symmetry. The rotational symmetry of σ bonds of octagraphene is lower than that of graphene, and hence octagraphene is less stable than graphene. The remaining p orbital electrons form π bonds similar to those in graphene.

In Fig. 2(a), we show our DFT-calculated band structures with a variable lattice constant a. There are two bands, ϵ_2 and ϵ_3, near the Fermi level. For $a/a_0 = 0.9$, the bands are quadruple degenerate at point M with $E = -3.01$ eV. This coincidence is different from the Dirac point. The structure is not a biconical structure with linear dispersion, but a parabolic dispersion. This means that low-energy excitations are no longer massless.

At the Fermi level, the band structures contain a hole pocket around the Γ point and an electron pocket around the M point [see Fig. 2(b)]. This is similar to the undoped Fe-pnictide materials [41]. The two pockets connected by the

nesting vector $\mathbf{Q}_1 = (\pi, \pi)$ form the well FS nesting, which is independent of deformations within the single layer.

After the general procedure of Fourier transformation, the Hamiltonian, Eq. (1), of the single layer reads

$$
\widetilde{H}_1 = - \begin{bmatrix}
0 & t_1 & t_2 e^{ik_y} + t_3 & t_1 \\
t_1 & 0 & t_1 & t_2 e^{ik_x} + t_3 \\
t_2 e^{-ik_y} + t_3 & t_1 & 0 & t_1 \\
t_1 & t_2 e^{-ik_x} + t_3 & t_1 & 0
\end{bmatrix}.
\tag{11}
$$

We obtain four bands, ϵ_1, ϵ_2, ϵ_3, and ϵ_4, by diagonalizing Eq. (11). Since ϵ_1 and ϵ_4 are away from the Fermi level, we only use ϵ_2 and ϵ_3 to get better fittings. By fitting bands ϵ_2 and ϵ_3 of the path from point Γ to point M, we get $t_1 = 2.678 \pm 0.033$ eV, $t_2 = 2.981 \pm 0.027$ eV, and $t_3 = 0.548 \pm 0.024$ eV with $a/a_0 = 1.0$. In comparison, $t \approx 2.7$ eV for the nearest-neighbor hopping energy and $t' \approx 0.1$ eV for the next-nearest-neighbor hopping energy are reported for graphene [42]. Note that the existence of this small t_3 is necessary to split the ϵ_3 and ϵ_4 at point M and make ϵ_2 coincide with ϵ_3 here.

$\mathbf{Q}_1$ remains almost unchanged with different deformations [see Fig. 2(b)]. This is because the diagonalization result of Eq. (11) is mathematically independent of the deformation a/a_0. This phenomenon is also examined by our DFT calculation, supporting the credibility of our TB model. Such an unchanged FS nesting may stabilize the SC phase of the octagraphene.

Figure 2(c) shows the variable fitting parameters t_1, t_2, and t_3 of the TB model with lattice constant a. As the distances between carbon atoms increase, the values of t_1, t_2, and t_3 decrease. This leads to the flatter band structures in Fig. 2(a). However, t_2/t_1 remains almost 1.1 when a changes from $0.90a_0$ to $1.20a_0$. The relative interaction t_2/t_1 is independent of a. We may conclude that the hopping energies between carbon atoms are nearly inversely proportional to the distances based on our calculations.

We then use a Hubbard model in Eq. (2) to study the influence of spin fluctuation on SCs. Although the interaction parameter U would be more than 10 eV for graphene-based materials, the accurate value of U is still under discussion [42]. Due to the weak-coupling character of the RPA, there is a limitation on the value of U, i.e., U_c. Here, we set $U = 5.4$ eV ($2t_1$) and the electron doping density x is 10% according to our estimation of the limits of the RPA. The details of the RPA limitation U_c are elaborated in Sec. V. The diagonalizing eigensusceptibilities $\chi(\mathbf{q})$ of Eq. (3) peak at the vector $\mathbf{Q}_1 = (\pi, \pi)$, also verified by our DFT result. The related eigenvector of susceptibilities $\epsilon(\mathbf{Q}_1) = (1/2, -1/2, 1/2, -1/2)$ means that the Néel pattern is formed [see Fig. 4(d)].

We then get $\lambda = 0.321$ for $a/a_0 = 1.0$ and $T_c \sim 190$ K for the single-layer octagraphene. For comparison, it has been reported recently that the calculated T_c is 20.8 K within the framework of electron-phonon coupling [27]. Our calculated T_c is much higher due to the spin fluctuation, not the electron-phonon interaction. In the previous study, our variational Monte Carlo gives the superconducting gap amplitude $\Delta \approx 50$ meV and a similar T_c at ~ 180 K with
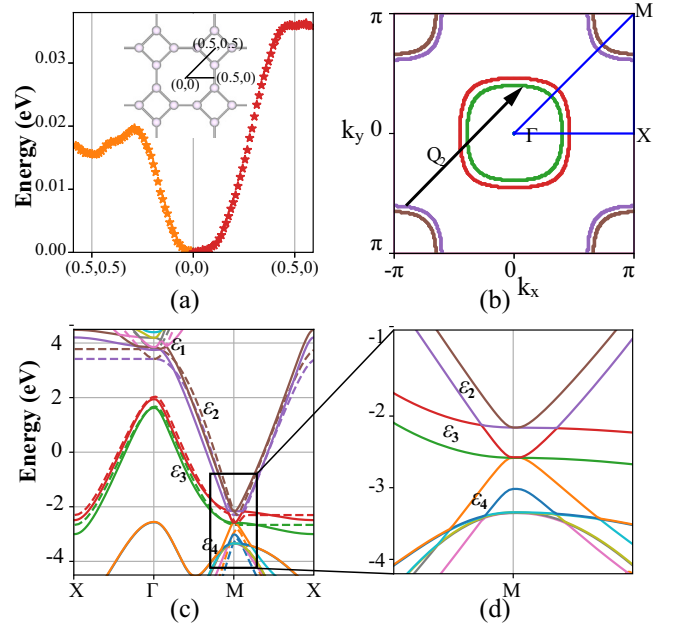

FIG. 3. (a) Differences between the cohesive energy per atom of bilayer octagraphene with relative shifts. Relative shifts between the two layers are chosen along (100) and (110) in real space. A-A stacking (0,0) is the most stable in our calculation. (b) Fermi surface of bilayer octagraphene. The nesting vectors $\mathbf{Q}_2 = (\pi, \pi)$, $(\pi + \delta, \pi + \delta)$, and $(\pi - \delta, \pi - \delta)$ indicate the deviation from perfect Fermi surface nesting. (c) Band structures of bilayer octagraphene with $a_0 = 3.45$ Å. Solid lines represent the results by DFT calculation. Dashed lines are fitting results of the TB model. (d) Detailed bands near point M. Three branches from ϵ_2, ϵ_3, and ϵ_4 coincide and form a triple degeneracy at the M point.

the $s^{\pm}$-wave pairing [26]. The consistence between the two methods shows great potential to search for high-T_c superconductors.

We also note that with a decrease in a, T_c decreases on a limited scale. This may be explained by the weakness of interactions. However, T_c will remain at a high value (> 100 K) when a/a_0 increases from 0.9 to 1.2. Thus the single-layer octagraphene would be a good superconductor with limited mechanical deformation.

IV. MULTILAYER OCTAGRAPHENE

In real materials, multilayer octagraphene may be more common. We here apply a DFT + RPA method to study the properties of multilayer octagraphenes. We first verify the stacking modes of bilayer octagraphene. Due to the C_{4v} symmetry of single layers, there may be three most probable stacking modes between two octagraphene layers—A-A stacking, A-B stacking, and A-C stacking—which are defined as (0, 0), (0.5, 0.5), and (0, 0.5) relative shifts between the two layers, respectively. The differences between the cohesive energy per atom along the (100) and (110) directions are shown in Fig. 3(a). In our calculations, A-A (0,0) stacking is the most stable. Otherwise, from A-A (0,0) stacking to A-B (0.5, 0.5) stacking, the energy differences are smaller compared with those for graphene. The distance between the neighboring
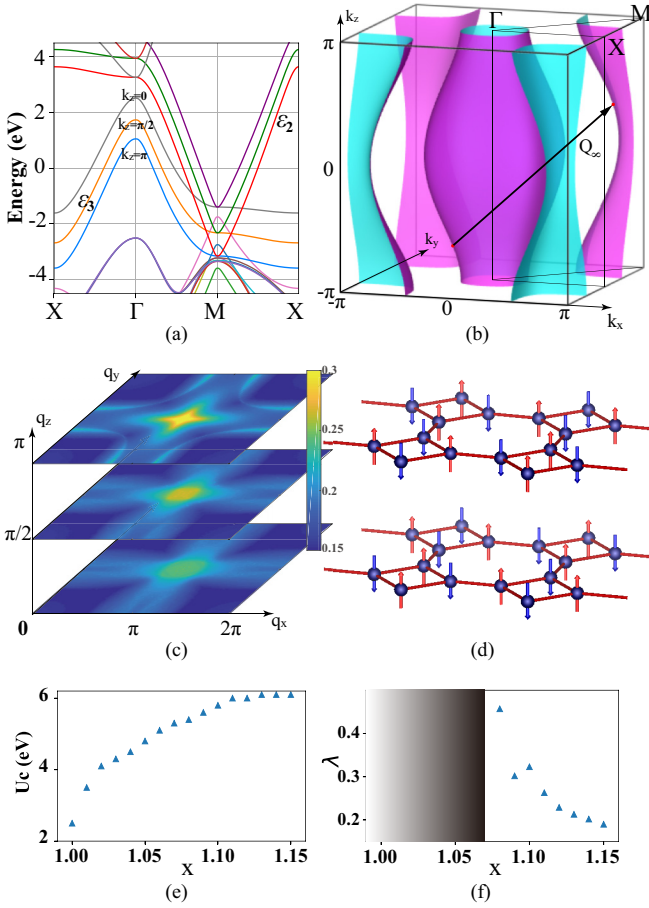
TABLE I. Lattice constant a_0, fitting parameters t_1, t_2, t_3, and $t_\perp$, and λ of single- to six-layer octagraphene and octagraphite (∞).

n	a_0 (Å)	t_1 (eV)	t_2 (eV)	t_3 (eV)	$t_\perp$ (eV)	λ
1	3.444	2.678(33)	2.980(27)	0.548(24)	—	0.330
2	3.446	2.685(21)	3.001(16)	0.558(16)	0.184(11)	0.324
3	3.447	2.680(16)	2.994(13)	0.548(12)	0.222(07)	0.320
4	3.446	2.678(13)	3.001(11)	0.550(11)	0.263(06)	0.320
5	3.447	2.671(12)	2.993(10)	0.546(09)	0.261(05)	0.320
6	3.449	2.677(11)	2.999(09)	0.548(08)	0.247(05)	0.313
∞	3.447	2.686(17)	2.986(13)	0.574(12)	0.259(05)	0.319

FIG. 4. Octagraphite. (a) Band structures with $k_z = 0$, $\pi/2$, π. (b) Fermi surface obtained by VESTA [44]; the nesting vector is almost $\mathbf{Q}_\infty = (\pi, \pi, \pi)$. (c) Eigensusceptibilities $\chi(\mathbf{q})$ with $\mathbf{q}_z = 0$, $\pi/2$, π. $\chi(\mathbf{q})$ peaks at almost $\mathbf{Q}_\infty = (\pi, \pi, \pi)$. (d) Predicted antiferromagnetic Néel pattern with half-filling. (e) RPA-calculated U_c as a function of the electron doping density x. (f) Doping density x dependence of the largest pairing eigenvalues λ with $U = 5.4$ eV. Based on (e) and (f), we set $U = 5.4$ eV ($2t_1$) and electron doping density $x = 10\%$.

layers of multilayer octagraphene is 3.72 Å, which is larger than the value of graphene (3.4 Å). This indicates a weaker interlayer coupling, making the material more slippery than graphite [43].

Since the A-A stacking bilayer is the most stable stacking mode, we only consider the A-A stacking structure. The bilayer Hamiltonian near the Fermi surface in matrix form reads as

$$\widetilde{H}_2 = \begin{bmatrix} \widetilde{H}_1 & t_\perp \widetilde{I}_{4\times4} \\ t_\perp \widetilde{I}_{4\times4} & \widetilde{H}_1 \end{bmatrix}, \qquad (12)$$

where $\widetilde{H}_1$ is Eq. (11) and $\widetilde{I}_{4\times4}$ is a 4×4 identity matrix.

The fitting parameters of bilayer octagraphene are $t_1 = 2.685 \pm 0.021$ eV, $t_2 = 3.001 \pm 0.016$ eV, $t_3 = 0.558 \pm 0.016$ eV, and $t_\perp = 0.184 \pm 0.011$ eV. t_1, t_2, and t_3 show little difference from those of single-layer octagraphene. This can be understood by the small interlayer interaction $t_\perp$, smaller than that of graphene ($t_\perp \approx 0.4$ eV) [42]. However, each band of the single layer splits into two bands due to the doubled unit

cell. As a result, there are two nesting hole pockets around the Γ point and two nesting electron pockets around the M point [see Fig. 3(b)].

Interestingly, three branches from ϵ_2, ϵ_3, and ϵ_4 coincide and form a triple degeneracy at point M [see Figs. 3(c) and 3(d)]. This triple degeneracy, which naturally exists in bilayer octagraphene, does not need any external deformation. From our TB model, the diagonalization of Eq. (12) gives exactly the same result at the M point when $t_1 + t_\perp = t_2 + t_3$ is satisfied. While the matching of single-layer ϵ_2 and ϵ_3 at the M point is determined by the C_{4v} symmetry, the matching with ϵ_4 is just a coincidence.

The usage of RPA for bilayer octagraphene gives $\lambda = 0.324$ for $U = 5.4$ eV, doping $x = 10\%$, which shows little difference from single-layer octagraphene. We obtain $T_c \sim 180$ K, which is a bit lower than that in single-layer octagraphene. We suppose that this may be caused by the interlayer interaction and cell expansion. Although $t_\perp$ is very small compared with the intralayer interactions, the well FS nesting of one layer deviates due to the interlayer interaction [see Fig. 3(b)]. There are two hole and two electron pockets with the nesting vectors $\mathbf{Q}_2 = (\pi, \pi)$, $(\pi + \delta, \pi + \delta)$, and $(\pi - \delta, \pi - \delta)$. The blurring of perfect FS nesting suppresses the superconductivity and reduces T_c.

Now we study the tendency of SCs with increasing layer numbers n. The A-A stacking multilayer octagraphenes show more 2D-like behavior. As n increases, the two energy bands ϵ_2 and ϵ_3 split into more branches due to the expansion of the unit cell. We can still use the same form of Eq. (12), which can be written as

$$\widetilde{H}_n = \begin{bmatrix} \widetilde{H}_1 & t_\perp \widetilde{I}_{4\times4} & & 0 \\ t_\perp \widetilde{I}_{4\times4} & \widetilde{H}_1 & t_\perp \widetilde{I}_{4\times4} & \\ & \ddots & \ddots & \ddots \\ 0 & & t_\perp \widetilde{I}_{4\times4} & \widetilde{H}_1 \end{bmatrix}. \qquad (13)$$

We fit the DFT-calculated data for ϵ_2 and ϵ_3 of the path from point Γ to point M to Eq. (13). The fitting parameters and λ of three to six layers are reported in Table I. We find that the fitting parameters are very close to those of bilayer octagraphene, whose relative differences are all less than 1%.

With increasing layer number n, we find that the pairing symmetry remains unchanged as $s^\pm$, and T_c does not change much. According to our estimation, we get $T_c \sim 170$ K for three to five layers and $T_c \sim 160$ K for six layers when $U = 5.4$ eV and doping $x = 10\%$. Thus we suggest that

superconductivity of octagraphene is related to the 2D characteristics of materials.

V. OCTAGRAPHITE

Similarly to graphite, it is important to study octagraphite ($n = \infty$). The DFT-calculated intralayer structure is similar to that of single-layer octagraphene, with only a slightly enhanced lattice size, as the interaction between the neighboring layers changes the lattice parameters slightly.

Figure 4(a) shows the DFT-calculated band structure of octagraphite. There are always four bands near the Fermi level for a given k_z, which shows the 2D feature of octagraphene materials. The highest and lowest boundaries of each band are labeled $k_z = 0$ and $k_z = \pi$, respectively. The 3D Fermi surface is fusiform, where the largest hole pocket is around the Γ point [see Fig. 4(b)]. It is similar to the multiorbital Fe-based superconductor family [41] and shows the importance of interlayer interactions.

We here use the 3D single-orbital TB model [Eq. (1)] to construct the major band features of octagraphite, which is given by

$$
\widetilde{H}_\infty = - \begin{bmatrix} 2t_\perp \cos k_z & t_1 & t_2 e^{ik_y} + t_3 & t_1 \\ t_1 & 2t_\perp \cos k_z & t_1 & t_2 e^{ik_x} + t_3 \\ t_2 e^{ik_y} + t_3 & t_1 & 2t_\perp \cos k_z & t_1 \\ t_1 & t_2 e^{-ik_x} + t_3 & t_1 & 2t_\perp \cos k_z \end{bmatrix}.
$$
(14)

Since ϵ_1 and ϵ_4 are away from the Fermi level, we only use ϵ_2 and ϵ_3 with $k_z = 0$, $\pi/2$, and π in our fittings. By fitting bands ϵ_2 and ϵ_3 from point Γ to point M, we get $t_1 = 2.686 \pm 0.017$ eV, $t_2 = 2.986 \pm 0.013$ eV, $t_3 = 0.574 \pm 0.012$ eV, and $t_\perp = 0.259 \pm 0.005$ eV. $t_\perp$ here shows little difference from octagraphene with layer number $n \geqslant 4$.

We now need to consider the form of the Fermi surface. See Fig. 1(c) from the TB model, Eq. (1). $(c_{1\sigma}, c_{2\sigma}, c_{3\sigma}, c_{4\sigma})$ in a unit cell can be transformed to $(-c_{1\sigma}, c_{2\sigma}, -c_{3\sigma}, c_{4\sigma})$ with a gauge transformation $\widetilde{T}$, as

$$
\widetilde{T} H_{\text{TB}}(t_1, t_2, t_3, t_\perp) \widetilde{T}^{-1} = H_{\text{TB}}(-t_1, t_2, t_3, t_\perp). \quad (15)
$$

Since the gauge transformation $\widetilde{T}$ does not change the momentum coordinates, $H_{\text{TB}}(t_1, t_2, t_3, t_\perp)$ has exactly the same energy levels as $H_{\text{TB}}(-t_1, t_2, t_3, t_\perp)$ at any momentum **k**.

It is easily seen that when $t_3 = 0$ in Eq. (14), $\widetilde{H}_\infty(\mathbf{k})$ and $\widetilde{H}_\infty(\mathbf{k} + (\pi, \pi, \pi))$ satisfy the following equations:

$$
\widetilde{H}_\infty(\mathbf{k}, t_1, t_2, t_\perp) = -\widetilde{H}_\infty(\mathbf{k} + (\pi, \pi, \pi), -t_1, t_2, t_\perp). \quad (16)
$$

Given that the eigenvalues of $\widetilde{H}_\infty(\mathbf{k})$ and $\widetilde{H}_\infty(\mathbf{k} + (\pi, \pi, \pi))$ have the same absolute value with a different sign, consider, for simplicity, that all energy levels in a Brillouin half-zone must have values opposite to those of the other half. Therefore, the Fermi energy level is located at $E_f = 0$ with half-filling exactly. If eigenvalue $E_\mathbf{k} = 0$ occurs at a nonspecific **k**, $E_\mathbf{k}$ at the Fermi energy level, it is easily seen that $E_{\mathbf{k}+(\pi,\pi,\pi)} = 0$. We finally prove the perfect FS nesting vector $\mathbf{Q}_\infty = (\pi, \pi, \pi)$ for $t_3 = 0$ in Eq. (14). When $t_3 > 0$, the actual FS nesting vector deviates from $\mathbf{Q}_\infty = (\pi, \pi, \pi)$ on a limited scale.

Figure 4(c) shows the eigensusceptibilities $\chi(\mathbf{q})$ for $q_z = 0$, $\pi/2$, π. $\chi(\mathbf{q})$ peaks at $\mathbf{Q}_\infty = (\pi, \pi, \pi)$, and the related eigenvector of susceptibilities $\epsilon(\mathbf{Q}_\infty) = (1/2, -1/2, 1/2, -1/2)$ means that the Néel pattern is obtained both within the layer and between the layers with half-filling, shown in Fig. 4(d). The reason that $\chi(\mathbf{q})$ peaks at $\mathbf{Q}_\infty = (\pi, \pi, \pi)$ lies in the fact that the FS nesting vector is at $\mathbf{Q}_\infty = (\pi, \pi, \pi)$. As shown in Fig. 4(b), due to the interlayer coupling, the hole pocket centering at the Γ point is no longer nested with the electron pocket centered at the M $(\pi, \pi, 0)$ point with the same k_z, and instead it is best nested with the electron pocket centered at the (π, π, π) point. Therefore, the FS nesting vector is $\mathbf{Q}_\infty = (\pi, \pi, \pi)$. Note that such an interlayer magnetic structure is new for octagraphite and is absent for single-layer octagraphene. What is more, the FS nesting in this case is not perfect, which leads to a small but finite U_c with half-filling [see Fig. 4(e)]. This means that considerable superconductivity can occur even at half-filling.

Finally, we get $\lambda = 0.319$ and $T_c \sim 170$ K for octagraphite. Practically, the U values of real carbon-based materials are larger than our given value, $U = 5.4$ eV [45]; this may provide a chance to get a higher T_c in real materials. However, the RPA-given T_c level is usually overestimated because of its weak-coupling perturbation, with its limitation of adopting a strong U [40]. As shown in Fig. 4(e), the RPA-limited U_c is above 6.0 eV when the electron doping density $x > 10\%$. In Fig. 4(f), the dependence of x on λ shows that the RPA results are reliable when U/U_c is far less than 1. Thus we set $U = 5.4$ eV and $x = 10\%$ to approach a relatively reasonable T_c in the field of our RPA limit.

We note that the λ of octagraphite shows a small decrease from that of single-layer octagraphene. Note that t_3 here is larger than that of single-layer octagraphenes and is negative to form the well nesting FS. The Fermi nesting deviates due to the interlayer interaction, leading to a small decrease in T_c. The calculated $s^\pm$-wave pairing is stronger than the other three pairing symmetry channels (p, d_{xy}, $d_{x^2-y^2}$), so the superconductivity of octagraphite is also similar to multiorbital Fe-based superconductors. In addition, the λ of octagraphite converges to a constant value when the layer number $n \geqslant 3$, which means that T_c changes little with n. This reflects the 2D nature of octagraphite.

Interestingly in Figs. 2(a), 3(c), and 4(a), except for the four energy bands described by the TB model, other bands are almost the same and independent of the layer number n from the DFT results. They are represented by the local properties of orbits. Note that these bands are far away from the Fermi level, so they have little influence on the superconductivity.

VI. CONCLUSIONS

Here we study the electronic structure, magnetism, and superconductivity of single-layer octagraphene, multilayer octagraphene, and octagraphite. DFT calculations suggest that multilayer octagraphene has a simple A-A stacking and the cohesive energy differences are smaller than those of graphene. This indicates a good slip property and promising mechanical applications. A TB model is built to capture the main features for each layer number n. The hopping parameters are obtained with a high accuracy. We find that the

hopping parameters change little with the layer number n. The van der Waals interaction induces $t_\perp \approx 0.25$ eV, smaller than for multilayer graphenes. All these findings support that multilayer octagraphene and octagraphite are more 2D-like. We find a sandwich structure with multiple energy bands overlapping frequently in multilayer octagraphene. This band structure has not been reported before, which may reveal more interesting topological phenomena.

At the Fermi level, the band structures of octagraphenes contain hole pockets around the Γ point and electron pockets around the M point. The two pockets connected by the nesting vector $\mathbf{Q}_1 = (\pi, \pi)$ form the well Fermi-surface nesting for single-layer octagraphene. For multilayer octagraphene the nesting vector is blurred from $\mathbf{Q} = (\pi, \pi)$, which makes T_c lower than that for single-layer octagraphene. For octagraphite, Fermi-surface nesting is switched to a 3D form with nesting vector $\mathbf{Q}_\infty = (\pi, \pi, \pi)$, also yielding a high T_c.

By applying the RPA method with half-filling, a 3D antiferromagnetic Néel magnetism is obtained both within layers and between layers. Thus spin fluctuation is dominant for the SC pairing with doping. We calculate the T_c of single-layer octagraphene, multilayer octagraphene, and octagraphite and find that the interlayer interaction does not affect the superconducting state much. With increasing n, T_c converges to $\sim$170 K, which is still high. The difference between three-layer octagraphene and octagraphite is so tiny that we suggest that the high-temperature

superconducting $s^\pm$ pairing mechanism of this material is mainly a 2D mechanism.

Moreover, we find that in-plane strain or stress does not change the energy bands obviously near the Fermi surface for single-layer octagraphene. As an actual single-layer octagraphene may exist on a substrate, the lattice difference with the substrate would lead to some deformations. Therefore, this stability of Fermi nesting may confer great advantages for preparation. We note that the synthesis of multilayer octagraphene is now in progress. Novel synthesis routes of multilayer octagraphene have been reported recently [27]. One-dimensional carbon nanoribbons with four- and eight-membered rings have been synthesized experimentally [28]. This holds great hope for realization of this promising high-T_c material in the future.

[1] Q.-Y. Wang, Z. Li, W.-H. Zhang, Z.-C. Zhang, J.-S. Zhang, W. Li, H. Ding, Y.-B. Ou, P. Deng, K. Chang, J. Wen, C.-L. Song, K. He, J.-F. Jia, S.-H. Ji, Y.-Y. Wang, L.-L. Wang, X. Chen, X.-C. Ma, and Q.-K. Xue, Chin. Phys. Lett. **29**, 037402 (2012).

[2] J. M. Lu, O. Zheliuk, I. Leermakers, N. F. Q. Yuan, U. Zeitler, K. T. Law, and J. T. Ye, Science **350**, 1353 (2015).

[3] X. Xi, Z. Wang, W. Zhao, J.-H. Park, K. T. Law, H. Berger, L. Forró, J. Shan, and K. F. Mak, Nat. Phys. **12**, 139 (2016).

[4] G.-Y. Zhu, F.-C. Zhang, and G.-M. Zhang, Phys. Rev. B **94**, 174501 (2016).

[5] Y. Yu, L. Ma, P. Cai, R. Zhong, C. Ye, J. Shen, G.-D. Gu, X.-H. Chen, and Y. Zhang, Nature **575**, 156 (2019).

[6] K. S. Novoselov, A. K. Geim, S. V. Morozov, D. Jiang, Y. Zhang, S. V. Dubonos, I. V. Grigorieva, and A. A. Firsov, Science **306**, 666 (2004).

[7] H. B. Heersche, P. Jarillo-Herrero, J. B. Oostinga, L. M. K. Vandersypen, and A. F. Morpurgo, Nature (London) **446**, 56 (2007).

[8] M. Xue, G. Chen, H. Yang, Y. Zhu, D. Wang, J. He, and T. Cao, J. Am. Chem. Soc. **134**, 6536 (2012).

[9] K. Li, X. Feng, W. Zhang, Y. Ou, L. Chen, K. He, L.-L. Wang, L. Guo, G. Liu, Q.-K. Xue, and X. Ma, Appl. Phys. Lett. **103**, 062601 (2013).

[10] B. M. Ludbrook, G. Levy, P. Nigge, M. Zonno, M. Schneider, D. J. Dvorak, C. N. Veenstra, S. Zhdanovich, D. Wong, P. Dosanjh, C. Straßer, A. Stöhr, S. Forti, C. R. Ast, U. Starke, and A. Damascelli, Proc. Natl. Acad. Sci. USA, **112**, 11795 (2015).

[11] A. P. Tiwari, S. Shin, E. Hwang, S.-G. Jung, T. Park, and H. Lee, J. Phys.: Condens. Matter **29**, 445701 (2017).

[12] L. Huder, G. Trambly de Laissardiére, G. Lapertot, A. Jansen, C. Chapelier, and V. Renard, Carbon **140**, 592 (2018).

[13] M. Calandra and F. Mauri, Phys. Rev. Lett. **95**, 237002 (2005).

[14] Y. Cao, V. Fatemi, S. Fang, K. Watanabe, T. Taniguchi, E. Kaxiras, and P. Jarillo-Herrero, Nature (London) **556**, 43 (2018).

[15] M. Calandra, G. Profeta, and F. Mauri, Phys. Status Solidi B Basic Res. **249**, 2544 (2012).

[16] J. Pešić, R. Gajić, K. Hingerl, and M. Belić, Europhys. Lett. **108**, 67005 (2014).

[17] T. P. Kaloni, A. V. Balatsky, and U. Schwingenschlögl, Europhys. Lett. **104**, 47013 (2013).

[18] I. I. Mazin and A. V. Balatsky, Philos. Mag. Lett. **90**, 731 (2010).

[19] C. Si, Z. Liu, W. Duan, and F. Liu, Phys. Rev. Lett. **111**, 196802 (2013).

[20] B.-T. Wang, P.-F. Liu, T. Bo, W. Yin, O. Eriksson, J. Zhao, and F. Wang, Phys. Chem. Chem. Phys. **20**, 12362 (2018).

[21] D. Malko, C. Neiss, F. Viñes, and A. Görling, Phys. Rev. Lett. **108**, 086804 (2012).

[22] T. Morshedloo, M. R. Roknabadi, M. Behdani, M. Modarresi, and A. Kazempour, Comput. Mater. Sci. **124**, 183 (2016).

[23] Y. Liu, G. Wang, Q. Huang, L. Guo, and X. Chen, Phys. Rev. Lett. **108**, 225505 (2012).

[24] X.-L. Sheng, H.-J. Cui, F. Ye, Q.-B. Yan, Q.-R. Zheng, and G. Su, J. Appl. Phys. **112**, 074315 (2012).

[25] F. Crasto de Lima, G. J. Ferreira, and R. H. Miwa, Phys. Chem. Chem. Phys. **21**, 22344 (2019).

[26] Y.-T. Kang, C. Lu, F. Yang, and D. X. Yao, Phys. Rev. B **99**, 184506 (2019).

[27] J. S. Q. Gu and D. Xing, Chin. Phys. Lett. **36**, 097401 (2019).

[28] M. Liu, M. Liu, L. She, Z. Zha, J. Pan, S. Li, T. Li, Y. He, Z. Cai, J. Wang, Y. Zheng, X. Qiu, and D. Zhong, Nat. Commun. **8**, 14924 (2017).

[29] G. Kresse and J. Hafner, Phys. Rev. B **47**, 558 (1993).

[30] G. Kresse and D. Joubert, Phys. Rev. B **59**, 1758 (1999).

[31] G. Kresse and J. Hafner, Phys. Rev. B **49**, 14251 (1994).

[32] P. E. Blöchl, Phys. Rev. B **50**, 17953 (1994).

[33] J. P. Perdew, K. Burke, and M. Ernzerhof, Phys. Rev. Lett. **77**, 3865 (1996).

[34] S. Grimme, J. Antony, S. Ehrlich, and H. Krieg, J. Chem. Phys. **132**, 154104 (2010).

[35] J. Klimeš, D. R. Bowler, and A. Michaelides, J. Phys.: Condens. Matter **22**, 022201 (2009).

[36] M. Dion, H. Rydberg, E. Schröder, D. C. Langreth, and B. I. Lundqvist, Phys. Rev. Lett. **92**, 246401 (2004).

[37] K. Lee, É. D. Murray, L. Kong, B. I. Lundqvist, and D. C. Langreth, Phys. Rev. B **82**, 081101(R) (2010).

[38] W. J. Kim, M. Kim, E. K. Lee, S. Lebégue, and H. Kim, J. Phys. Chem. Lett. **7**, 3278 (2016).

[39] M. Kim, W. J. Kim, T. Gould, E. K. Lee, S. Lebegue, and H. Kim, J. Am. Chem. Soc. **142**, 2346 (2020).

[40] F. Liu, C.-C. Liu, K. Wu, F. Yang, and Y. Yao, Phys. Rev. Lett. **111**, 066804 (2013).

[41] P. J. Hirschfeld, M. M. Korshunov, and I. I. Mazin, Rep. Prog. Phys. **74**, 124508 (2011).

[42] A. H. Castro Neto, F. Guinea, N. M. R. Peres, K. S. Novoselov, and A. K. Geim, Rev. Mod. Phys. **81**, 109 (2009).

[43] Z. Liu, Nanotechnology **25**, 075703 (2014).

[44] K. Momma and F. Izumi, J. Appl. Crystallogr. **44**, 1272 (2011).

[45] M. Schüler, M. Rösner, T. O. Wehling, A. I. Lichtenstein, and M. I. Katsnelson, Phys. Rev. Lett. **111**, 036601 (2013).